Supplementary Information for "Phonon-Electron Interactions in Piezoelectric Semiconductor Bulk Acoustic Wave Resonators"

Vikrant J. Gokhale[1] and Mina Rais-Zadeh[1,2*]

Author Affiliations:
[1]Electrical Engineering and Computer Science Department, University of Michigan, Ann Arbor, Michigan 48109, USA
[1]Mechanical Engineering Department, University of Michigan, Ann Arbor, Michigan 48109, USA

[*]email: minar@umich.edu

I. Other loss mechanisms in PS-BAW resonators

The anharmonic phonon-phonon loss due to inelastic interaction of the acoustic wave with the lattice phonon can be expressed as[1]:

$$\alpha^{pp} = \begin{cases} \dfrac{C_v T \gamma^2 \tau}{2\rho s^3}\left(\dfrac{\omega^2}{1+\omega^2\tau^2}\right) & for\ \omega\tau < 1 \quad (Akhieser\ Regime) \\ \dfrac{\pi^5 \gamma^2 {K_b}^4 T^4}{30\rho s^6 h^3}\omega & for\ \omega\tau > 1 \quad (Landau - Rumer\ Regime) \end{cases}$$

The two regimes for phonon-phonon loss depend on whether one can consider the lattice to be interacting with phonon ensembles or individual phonons and are distinguished by the relation between the frequency and the phonon relaxation time τ.

Thermoelastic damping is due to the volume changes during vibrational motion that cause loss of energy as a result of the heat flow in the material. For longitudinal 'bar' resonators, such as those described in the main manuscript, operating at VHF/UHF frequencies with adiabatic vibration, the thermoelastic damping can be approximated to be[1]

$$\alpha^{TED} = \frac{\kappa T \beta^2 \rho}{18 {C_v}^2 s}\omega^2$$

Note that different values will apply for TED loss in flexural resonators and for purely shear mode resonators with isochoric vibration, there is ideally no TED loss.

The phonon relaxation time can be calculated from the equation[1]

$$\tau = \frac{3\kappa}{C_v s^2}$$

The reflection loss or interface loss is defined as the energy lost by the resonator through its tethers or through the air-interface surrounding it, as a consequence of non-ideal boundary conditions. This is not strictly a distributed bulk material loss; however, we model it as such for the purposes of fitting. Analytical solutions are difficult to achieve except for the simplest of situations, and so we use ξ and r as the fractions of energy lost and retained, respectively, per cycle of operation. $\xi + r = 1$. For the perfect resonant cavity of length L, $n\lambda = 2L$, $r = 1$, which implies perfect reflection and no loss at the material interface. For a real resonator, the presented model uses ξ as an independent parameter, ranging from 0.0001 to 0.01 in order to achieve a reasonable fit between the measured and modeled Q_m. The reflection loss coefficient is defined as[2]

$$\alpha^{reflection} = -\frac{1}{L}\ln\{r(\omega)\}$$

Phonon-electron interactions due to deformation potential coupling occur in all semiconductors[3] due to the perturbations of the conduction band due to lattice strain caused by phonons. The loss can be expressed as

$$\alpha_{DP}^{pe} = \frac{N\Xi^2}{9s^4 k_B T \rho} \frac{\omega^2 \tau_R (1-\eta)}{1+(1-\eta)^2 \omega^2 {\tau_R}^2}$$

where Ξ is the deformation potential constant, and τ_R is the relaxation time for intervalley transitions. In general, DP coupling is significantly smaller than piezoelectric coupling for low to moderate doped PS materials. DP coupling is the dominant phonon-electron interaction mechanism for non-piezoelectric semiconductors and semi-metals. A comparison for the calculated values of piezoelectric and DP coupling[4,5] for GaN confirms the dominance of piezoelectric coupling. The values for the various loss components in GaN are calculated using material properties from existing literature[4-8] (Table S1).

Table S1: Material properties used for calculating loss components for GaN

Material Property	Symbol	Values	Units	Ref.
Mass Density	ρ	6150	kg/m^3	[6]
Specific Heat	C_s	490	J/kg-K	[6]
Phonon Relaxation Time	τ	2.02×10^{-12}	s	-
Thermal Conductivity	κ	130	W/m-K	[6]
Coefficient of linear Expansion	β	5.6×10^{-6}	K^{-1}	[6]
Acoustic Velocity	s	8000	m/s	[6]
Grüneisen Parameter	γ	1.18	-	[7]
Deformation Potential Constant	Ξ	12	eV	[4,5]
Intervalley Relaxation Time	τ_R	1.2×10^{-12}	s	[8]

II. Analytical extraction of mechanical *Q*

The mechanical quality factor (Q_m) of a piezoelectric resonator can be calculated analytically by considering the lumped model of a single electroded region of the resonators and by using the relation

$$Q_m = \frac{\sqrt{km_{eff}}}{nR_m\zeta^2} = \frac{\omega m_{eff}}{nR_m\zeta^2}$$

This reduces to the relation between Q_m and motional resistance (R_m)

$$Q_m R_m = \frac{\omega m_{eff}}{n{\zeta_{ij}}^2}$$

This can be further simplified by using the relations

$$m_{eff} = \rho wlt/2$$

$$k_{33} = \frac{c_{33} w t}{l} \quad ; \quad k_{11} = \frac{c_{11} l t}{w}$$

$$\zeta_{33} = \frac{2 e_{33} w l}{t} \quad ; \quad \zeta_{31} = 2 e_{31} w$$

where ζ_{ij} is the electromechanical coupling coefficient (N/V), and n is the number of elemental resonators present in the entire device. The motional resistance (R_m) is the lumped representation of all the acoustic or mechanical losses in the system. The mass and the stiffness of the resonating element are described by the motional inductance (L_m) and motional capacitance (C_m), respectively, which are given by:

$$L_m = \frac{m_{eff}}{{\zeta_{ij}}^2} \quad ; \quad C_m = \frac{{\zeta_{ij}}^2}{\omega^2 m_{eff}}$$

The value of R_m can be extracted from the electrical impedance of the measured data, after considering the effect of electrical feedthrough and the parasitic capacitances originating in the device and contact pads.

For piezoelectric resonators, the only effective methods used for lowering R_m require optimization of the resonator geometry, electrode materials and dimensions, or the electrical/mechanical matching conditions[9]. Prior work on BAW resonators has focused on exhaustive analysis[10], low-loss designs[11], or improvement of material[12] and structural composition[13] to improve the *Q*. None of these improvements are dynamic in nature. It is seen in the current work that the values of R_m for the GaN resonators decrease significantly (up to 35% reduction), simply by applying a DC bias, indicating a reduction in the mechanical losses incurred. The improvement is dynamic, repeatable and reversible.

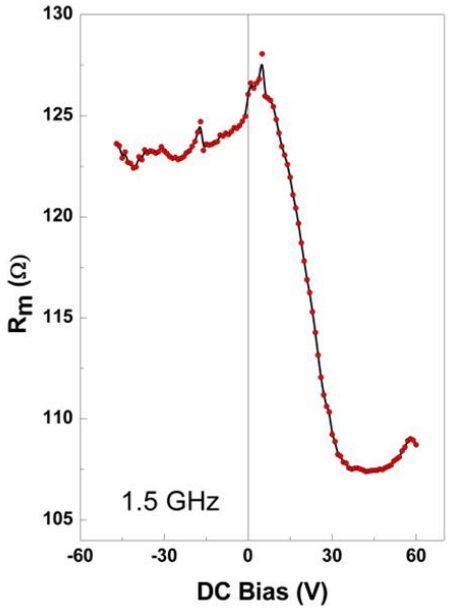

Figure S1: The values of $\boldsymbol{R_m}$ extracted from the measured data for the BAW device shown in Fig. 4 of the paper. The values of $\boldsymbol{Q_m}$ used in the paper are based on these extracted values.

The equivalent electrical model provides another corroborative indicator that R_m decreases with the applied electrical bias when all electrical parasitics are de-embedded. The exact values of the parasitics are calculated using the known dimensions of the GaN film and electrodes, and standard material properties of GaN from prior literature[6].

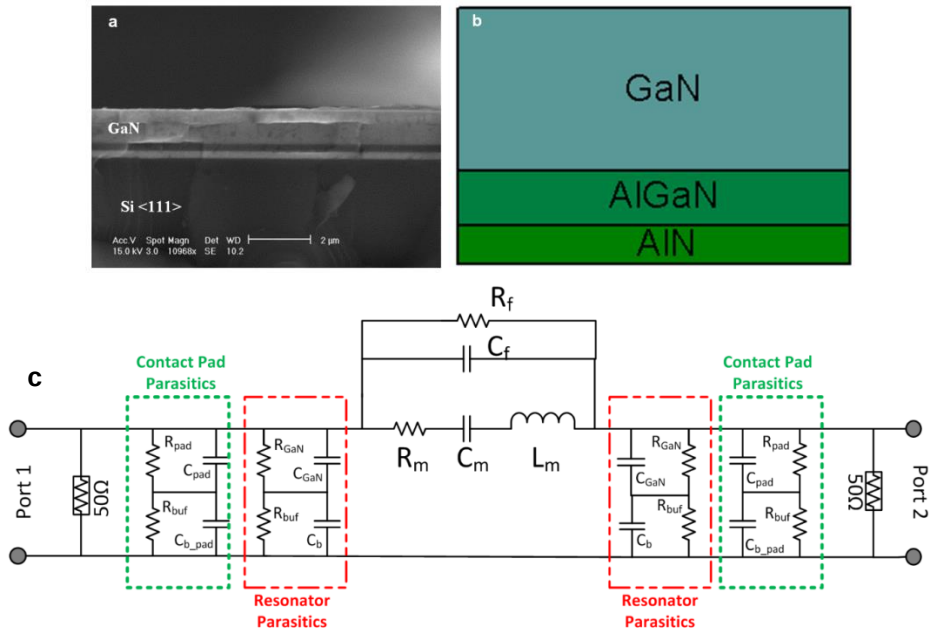

Figure S2: (a) Cross section electron micrograph of a GaN film epitaxially grown on a Si<111> wafer. (b) In order to mitigate the lattice mismatch between GaN and Si, a graded buffer layer consisting of AlN and AlGaN layers is customarily used. (c) A modified version of the two-port Butterworth-van Dyke (BVD) model of a resonator can be used to map mechanical quantities with their equivalent motional quantities. The parasitic effect of the buffer layers associated with the body of the resonator and the contact pads has been included for a more accurate fit. The model is symmetric with respect to its ports.

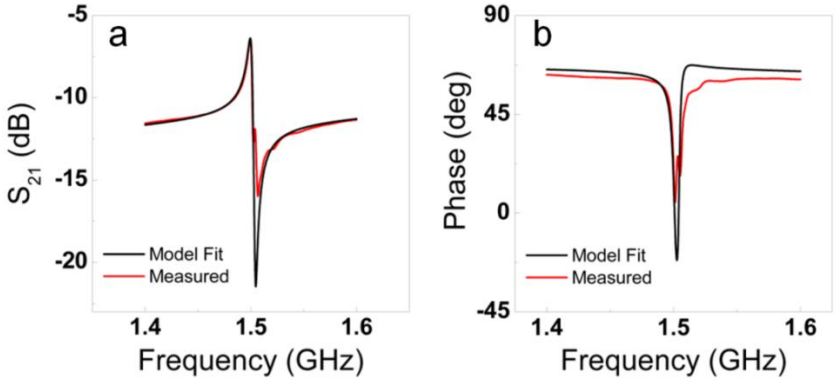

Figure S3: BVD model fit for the RF transmission magnitude and phase of the 1.5 GHz resonator shown in this work. It can be seen that the model provides an accurate match with measured RF transmission parameters. The lumped element values for the 1.5 GHz device used for this fitting are shown in Table S2. The transmission response of the resonator at each value of DC bias can be matched using the BVD model and corroborates the lowering of $\boldsymbol{R_m}$. The value of $\boldsymbol{R_m}$ for this resonator at varying DC bias is shown in Fig. S1.

Table S2: Dimensions and material properties used in the equivalent electrical model of the 1.5 GHz resonator

Material Properties							
Resistivity	GaN	0.0446	Ω-m	Relative Permittivity	GaN	8.9	-
	AlGaN	-	Ω-m		AlGaN	8.8	-
	AlN	-	Ω-m		AlN	8.5	-
Dimensions							
Film Thickness	GaN	1800	nm	In-plane Dimensions	L	130	μm
	AlGaN	250	nm		W	40	μm
	AlN	250	nm		L_{pad}	80	μm
					W_{pad}	80	μm
Parasitic Effects							
Resonator Parasitics	C(GaN)	40	fF	Pad Parasitics	C_{pad}(GaN)	40	fF
	R(GaN)	650	Ω		R_{pad}(GaN)	600	Ω
	C_b (AlGaN/AlN)	360	fF		C_{b_pad} (AlGaN/AlN)	300	fF
	R_{buf} (AlGaN/AlN)	$> 10^{12}$ (~open)	Ω		R_{buf} (AlGaN/AlN)	$> 10^{12}$ (~open)	Ω
Electrical Feedthrough							
Capacitance	C_f	374	fF	Resistance	R_f	17	kΩ
Motional Parameters							
Motional Capacitance	**Cm**	**1.875**	**fF**	**Motional Inductance**	**Lm**	**6**	**μH**

III. Comparison of experimental data and modeled values

The analytically modeled values for $Q_i{}^{total}$ are compared to the measured values for Q_m for the PS-BAW resonators. α_{SW}^{pe} is the only parameter that is dependent on applied E_D, and follows the trends shown in Fig. 2 of the paper. All loss mechanisms except $\alpha^{reflection}$ are calculated as discussed above. $\alpha^{reflection}$ is used as a fitting parameter to equate the nominal values of $Q_i{}^{total}$ and measured Q_m. Representative comparisons of PS-BAW resonators from each wafer are shown in Figure S4. The most critical parameters for achieving comparable trends are the resonant frequency and the effective electron concentration N. Unless otherwise noted, the values of μ and K^2 used in the calculations are 200 cm^2/V-s and 2 % respectively. All modeled values are for a temperature of 300 K. Resonators from the same wafer expectedly have the same values for N. For Wafers A and B respectively, the best comparison of N values are 1×10^{15} cm^{-3} and 7×10^{15} cm^{-3} respectively. For Wafer C, the amplification is low, and we use averaged data sets. The estimated value of N for Wafer C is $(8 \pm 2) \times10^{15}$ cm^{-3}. The gain saturation in Wafer C could be a result of higher trap density in GaN, non-linear response due to joule heating from DC current, or a combination of these effects. The high initial Q_m and the low amplification are as expected for a wafer with high doping. An accurate quantitative fit between modeled values and measured results is

not attempted at this point due to the large number of parameters involved in the loss component calculations, the large range of values for these parameters, and the fact that these values are derived from different sources in literature.

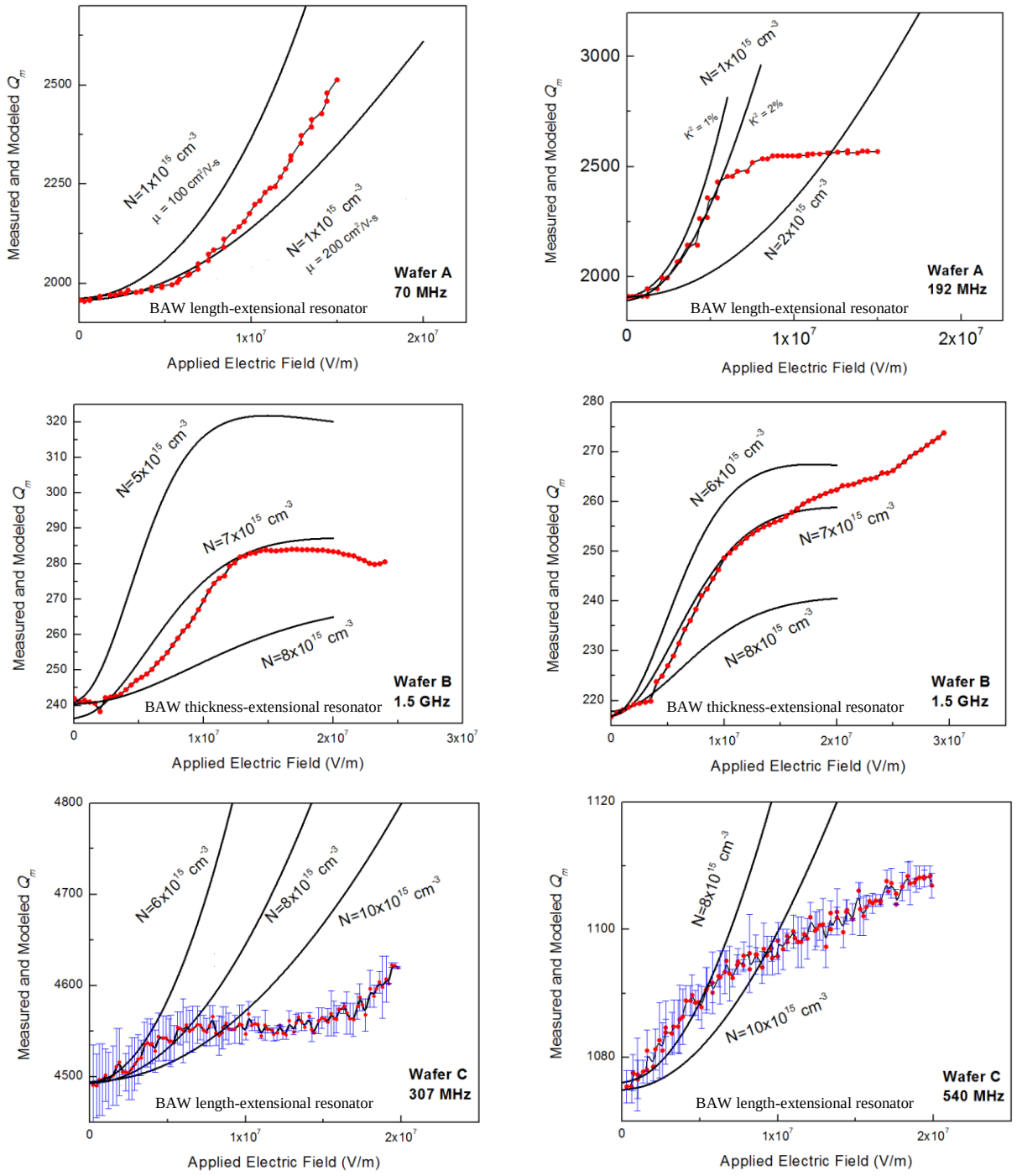

Figure S4: Qualitative comparison of the improvement in Q_m for representative resonators on multiple wafers, using the full intrinsic loss model. Approximate estimates for the effective electron concentrations of each wafer are determined using this comparison. Error bars for Wafer C denote the maximum/minimum data over multiple data sets for the same devices.

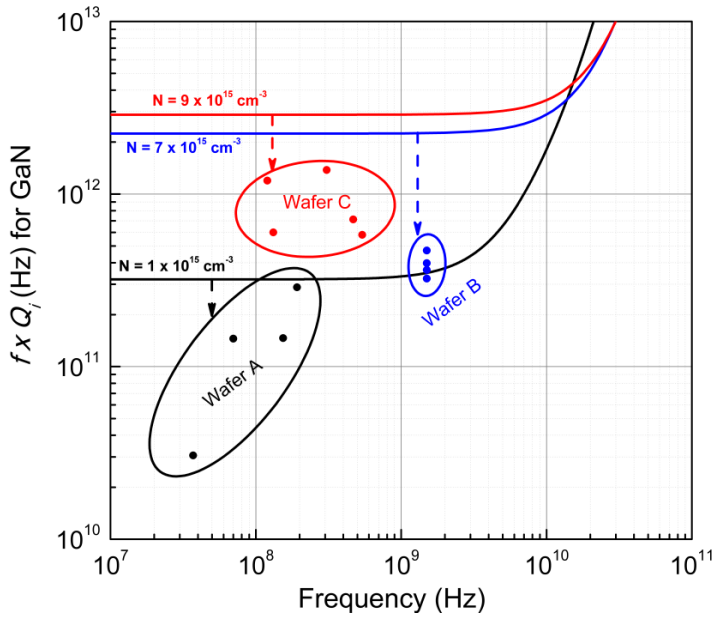

Figure S5: Measured values of $f \times Q$ for devices presented in Fig. 7 of the paper, and the limiting values imposed by the phonon-electron loss. The phonon-electron limits of $f \times Q$ depend on the specific values of N for each individual wafer. The difference between the $f \times Q$ limit and the measured values is due to reflection loss and other extrinsic losses not accounted for in the model. Reflection loss can be lowered by more optimized resonator design, while other losses can be reduced by reducing the defect density of the material lattice, operating the device in a vacuum and at low temperatures.

IV. Other materials

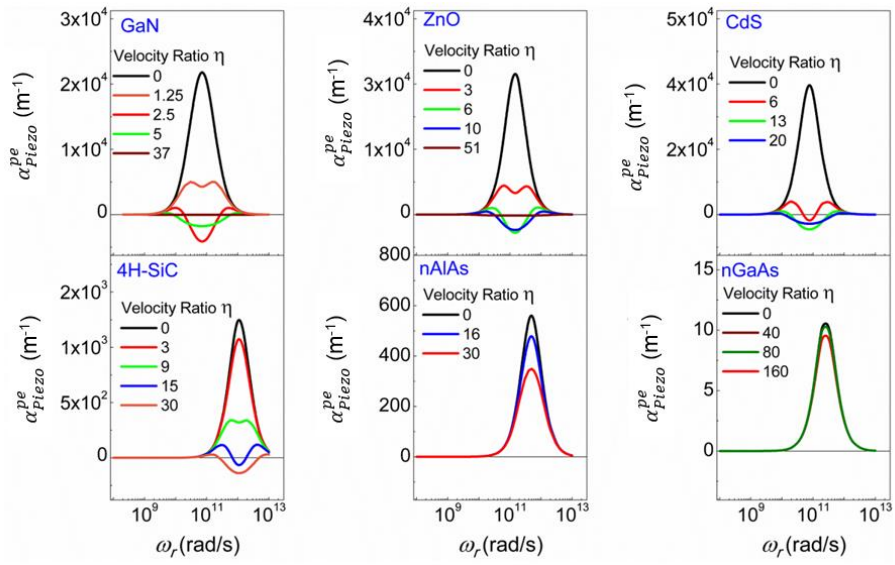

Figure S6: Potential PS materials for achieving acoustoelectrically amplified BAW resonators. Representative plots for $\alpha_{SW}^{pe}(\omega, \eta)$ for other PS materials that can potentially exhibit acoustoelectric amplification via piezoelectric interactions between phonons and electrons. Each material is investigated up to the limit η_{sat} set by the respective electron saturation velocity. Other loss mechanisms are not considered here. Material properties used for modeling are provided in Table S3. Note that the axes are scaled individually for visual clarity.

Numerical calculations are carried out for various candidate PS-BAW materials that may potentially exhibit acoustoelectric amplification via piezoelectric interactions between phonons and electrons (Fig. S6). The representative properties used for a comparison of these materials are provided in Table S3. Due to their higher piezoelectric coupling and lower N values, the wurtzite materials (GaN, ZnO, CdS, and 4H-SiC) exhibit a strong phonon-electron interaction and can transition into the gain regime. The velocity ratio η required to transition into the gain regime is low enough that the electron saturation velocity ratio η_{sat} is not exceeded. The cubic materials (AlAs and GaAs) exhibit a very weak reduction in phonon-electron loss due to low piezoelectric coupling and high N. The wurtzite materials are promising candidates for implementing BAW amplifiers. This model suggests that the piezoelectric mechanism for phonon-electron interaction is not sufficient for inducing acoustoelectric gain in the cubic materials. Note that α^{DP} may be a more significant interaction mechanism for the cubic semiconductors with weak piezoelectric coupling[3], but is not considered at this point. The wurtzite materials are more evenly matched in terms of acoustoelectric performance. Each material offers unique practical advantages such as high-quality epitaxially grown films (GaN), ease of deposition at low temperatures (ZnO, CdS) or low phonon-phonon loss (SiC)[14]. Prior work has shown acoustoelectric amplification in thick crystals of CdS[2] and ZnO[15] but the subsequent development of advanced processing technology makes it possible to practically design thin submicron films of GaN, CdS, ZnO, or SiC that can increase the fundamental thickness vibration frequency to the 1-10 GHz range, where acoustoelectric amplification can be seen most clearly in standing wave BAW resonators. Similarly, better control of growth or deposition can yield better quality films with tailored electronic properties. These materials can also be used in composite acoustic resonators or superlattices or integrated with electronics, leading to practical electromechanical systems that utilize acoustoelectric amplification to compensate for intrinsic material loss.

Table S3: Potential candidates for acoustoelectric amplification

	GaN	**ZnO**	**CdS**	**4H-SiC**	**AlAs**	**n-GaAs**	
Structure	Wurtzite	Wurtzite	Wurtzite	Wurtzite	Cubic	Cubic	units
K^2	0.02	0.217	0.03 - 0.07	8×10^{-4}	1.01×10^{-3}	3.7×10^{-4}	-
Mobility	150-440	150-200	285	400	180-294	1000 - 9000	$cm^2/V s$
Carrier Concentration	1×10^{15} - 1×10^{17}	6×10^{15} - 3×10^{16}	4×10^{15}	1×10^{17}	2×10^{17} - 9×10^{17}	1×10^{14} - 1×10^{19}	cm^{-3}
e_{ij}	0.65	0.96	0.385 - 0.626	0.2	-0.23	-0.16	C/m^2
ε_r	9	7.5	9.3 - 9.5	9.66	10.1	13.18	-
Acoustic Velocity	7960-8040	6200	4300 - 4500	13,100	2910	2470	m/s
Saturation Velocity	3×10^5	3.2×10^5	1×10^5	2.2×10^5	8.5×10^4	2×10^5	m/s
Ref.	6,16,17	18-20	6,21	6,22-24	25-27	25,26	

V. Fabrication Process

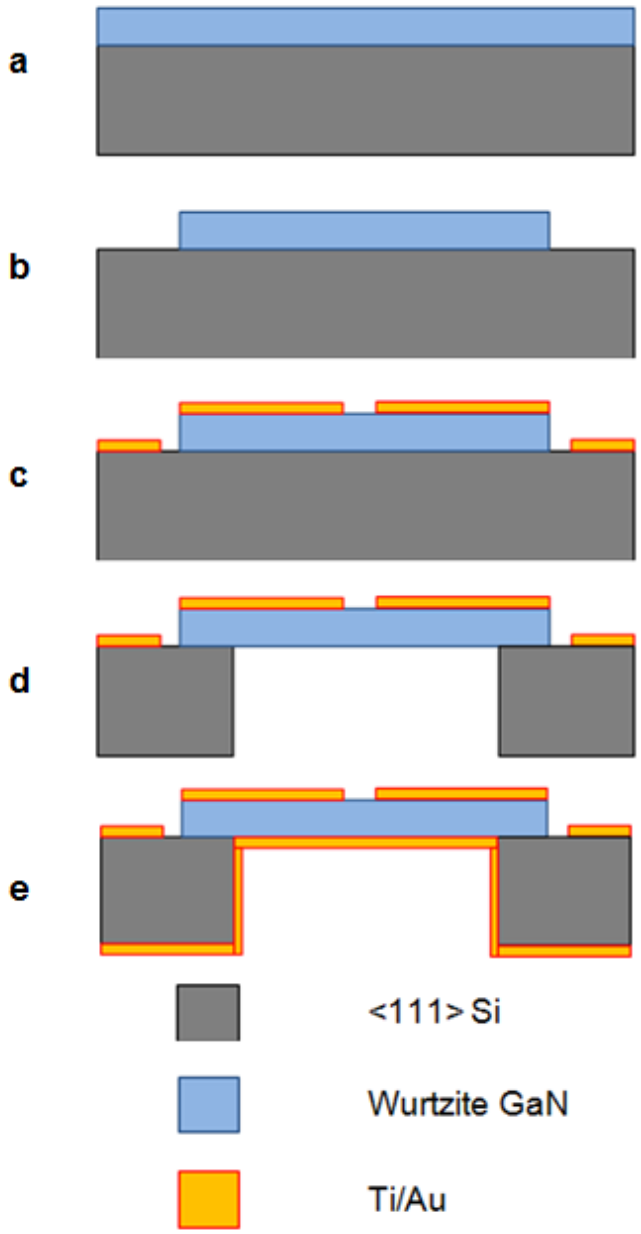

Figure S7: Fabrication process flow for thin film micromechanical BAW resonators using single crystal wurtzite GaN. (a) Initial GaN films (MOCVD or MBE) are grown on <111> Si wafers. AlN/AlGaN layers are used as buffer layers to alleviate the lattice mismatch and the resultant built-in stress between Si and GaN. (b) The GaN film (including the buffer layers) is lithographically patterned and plasma-etched using BCl_3/Cl_2 gas chemistry. (c)The top electrodes (Ti/Au, 10nm/100 nm respectively) are patterned onto the GaN resonators using electron beam evaporation and a liftoff process. (d) The GaN resonators are mechanically released using a back-side Si etch using deep reactive ion etching (DRIE). (e) The bottom electrode (Ti/Au, 10nm/100 nm respectively) is deposited on the back surface of the resonator using plasma sputtering for highly conformal and uniform coverage inside the DRIE trench.

VI. Experimental controls:

In order to validate the acoustoelectric effect as the causal phenomenon for the measured increase in *Q*, decrease in insertion loss, and reduction of bandwidth that is seen in the measured data for a large number of resonators, it is necessary to evaluate other possible electrical or mechanical causes. We investigate temperature, RF input power and non-linear I-V relations in GaN (Fig 8 from the main paper). The data from Fig. 8 are shown in more detail in figure S8-S10. Further, GaN is not ferroelectric[28], and poling of the films is not expected. Any possibilities of this amplification being a charging effect due to the presence of dielectric layers is negated by the fact that electric charges could only potentially change the transmission level but cannot amplify a specific mode selectively.

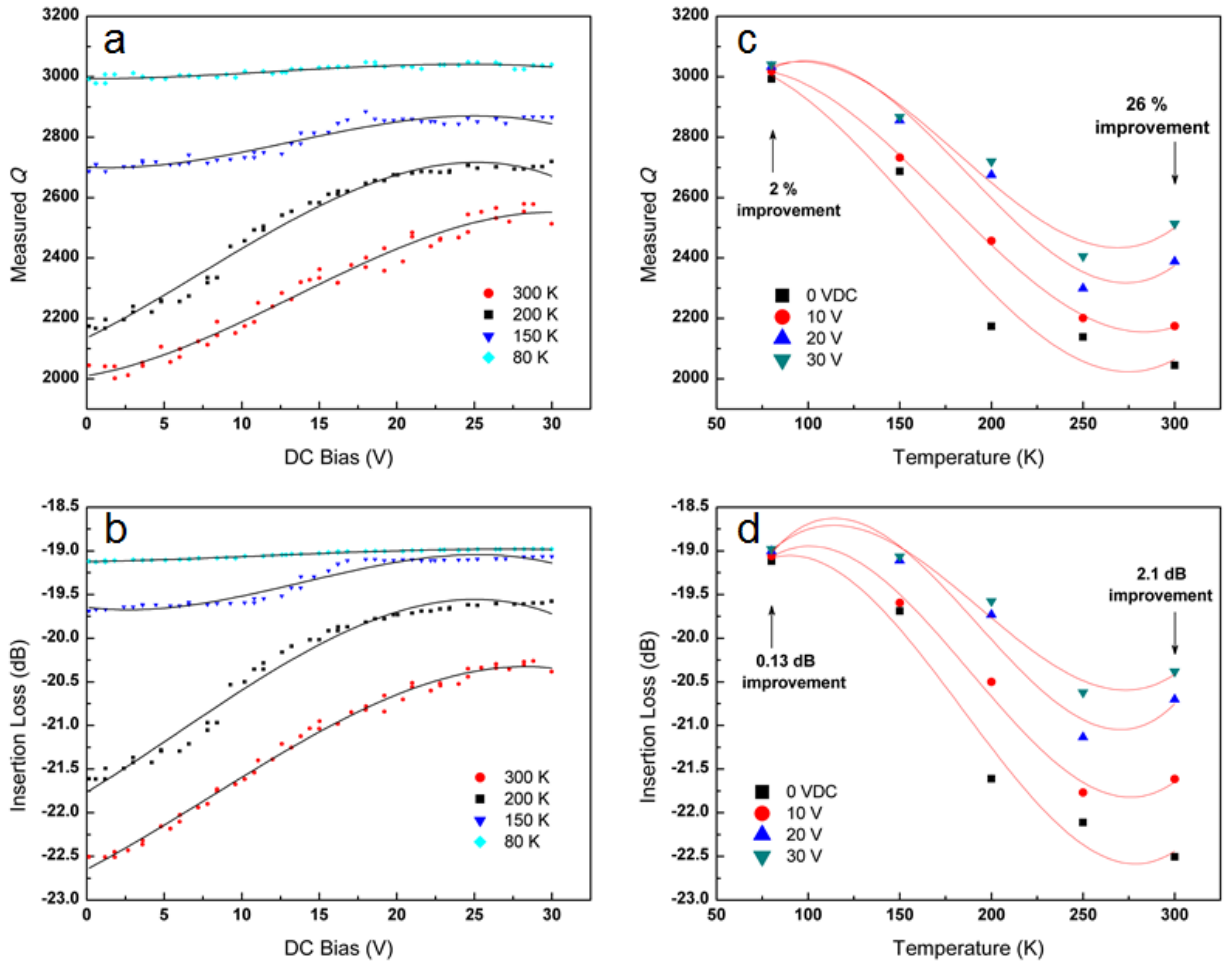

Figure S8: Change in (a) measured *Q* and (b) IL of a 70 MHz BAW resonator (Wafer A) with applied DC bias at various temperatures. We can see that elevated temperature reduces the *Q* and IL. (c) & (d) The same data plotted as a function of the temperature, at select values of DC bias. The reduction in *Q* improvement at low temperature needs further investigation. The data in (a) are replicated from Fig 8 in the main paper.

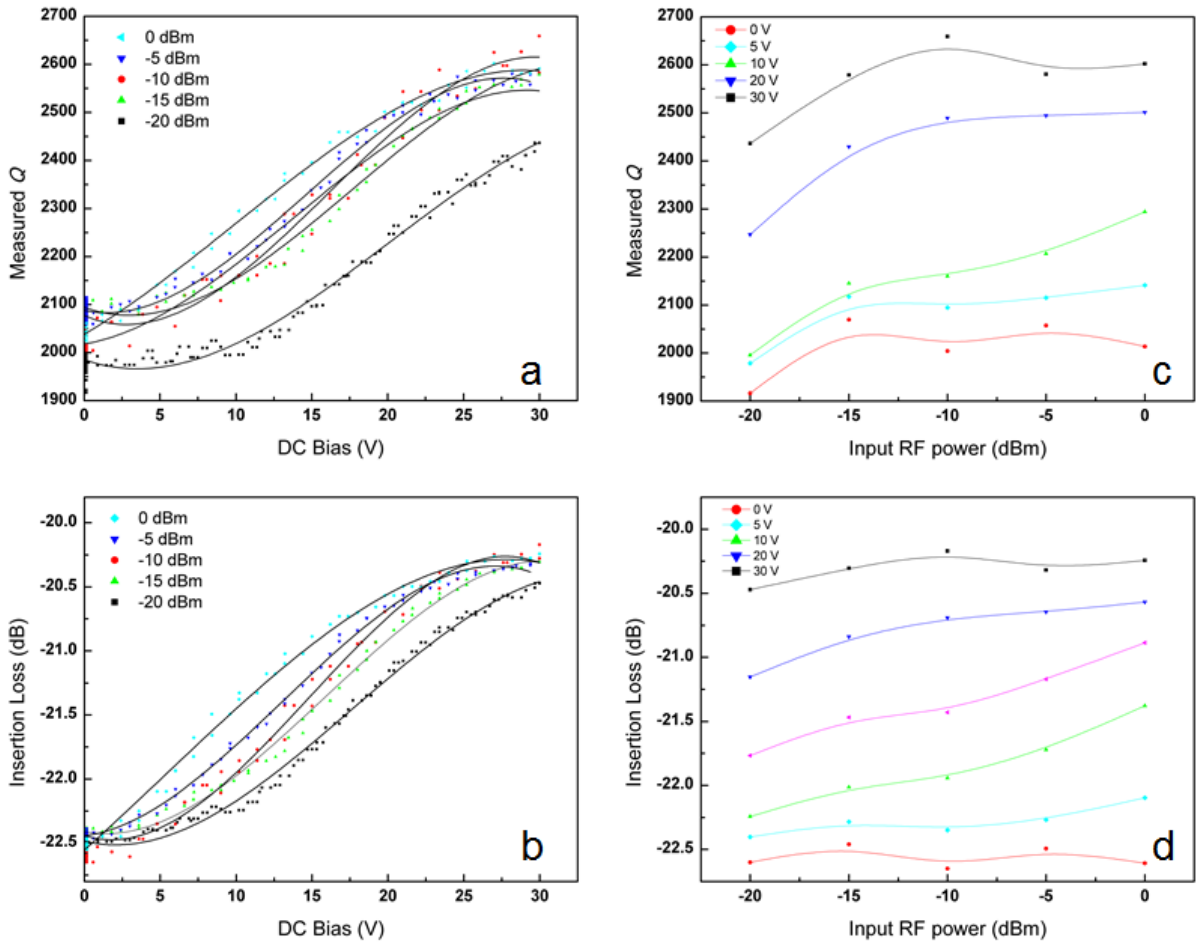

Figure S9: Change in (a) measured *Q* and (b) IL of the 70 MHz BAW resonator (Wafer A) with applied DC bias at different levels of RF input power. We can see that increasing the input power temperature improves the *Q* and IL slightly. (c) & (d) The same data plotted as a function of the RF power, at select values of DC bias. Increasing RF power improves performance slightly, but not significantly when compared to the DC bias. The data in (a) are replicated from Fig 8 in the main paper.

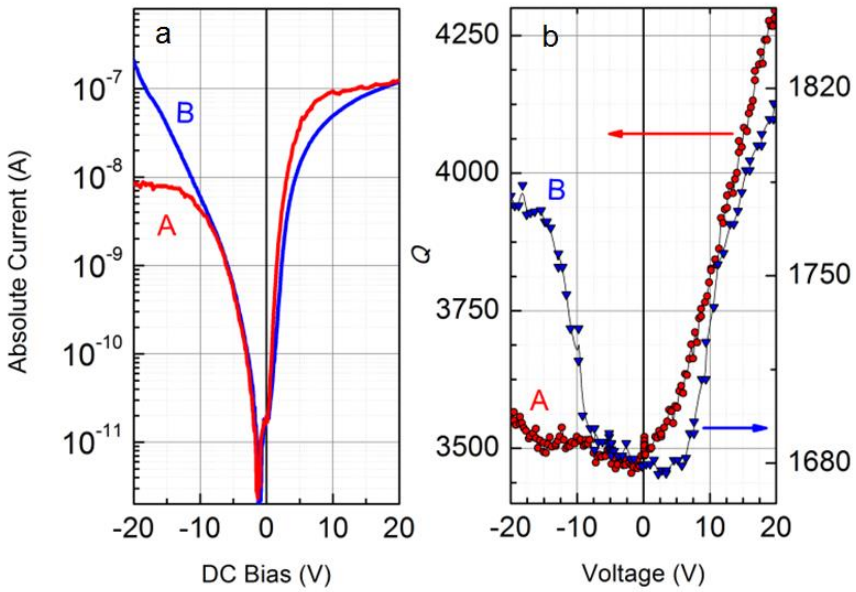

Figure S10: (a) DC I-V curves and (b) measured resonator *Q* for two similarly designed BAW resonators. In both cases, positive voltages result in similar trends in improvement of *Q*. In devices designated type A, a negative voltage results in negligible *Q* amplification, while in devices of type B, there is a perceptible change in the *Q* with a negative bias. This is well correlated with the nature of the DC current seen in both type of devices; devices that do not show large currents in the negative bias region do not show improvements in the *Q*. Further investigation into the n-GaN/Ti/Au contact is necessary to fully characterize and control the contact resistance and consequently the *Q* amplification with negative DC bias.

REFERENCES

1 Braginsky, V. B. & Mitrofanov, V. P. in *Systems with Small Dissipation* (ed Kip. S. Thorne) Ch. 1, 1-42 (The University of Chicago Press).

2 Maines, J. D. & Paige, E. G. S. High-frequency acoustoelectric currents and departures from Ohm's law in thin platelets of CdS I. Linear behaviour. *J.Phys. C* **2**, 175 (1969).

3 Pomerantz, M. Ultrasonic Loss and Gain Mechanisms in Semiconductors. *Proc. IEEE* **53**, 1438-1451, doi:10.1109/Proc.1965.4258 (1965).

4 Henriksen, E. A. *et al.* Acoustic phonon scattering in a low density, high mobility AlGaN/GaN field-effect transistor. *Appl. Phys. Lett.* **86**, 252108-252108-252103, doi:10.1063/1.1954893 (2005).

5 Chin, V. W. L., Tansley, T. L. & Osotchan, T. Electron mobilities in gallium, indium, and aluminum nitrides. *J. Appl. Phys.* **75**, 7365-7372, doi:http://dx.doi.org/10.1063/1.356650 (1994).

6 Siklitsky, V. *Semiconductors on NSM-Gallium Nitride*, <http://www.ioffe.ru/SVA/NSM/> (1998).

7 Perlin, P. *et al.* Raman scattering and x-ray-absorption spectroscopy in gallium nitride under high pressure. *Phys. Rev. B* **45**, 83-89 (1992).

8 Pavlidis, D. in *Optoelectronic Devices: III Nitrides* (eds M. Razeghi & M. Henini) 351-386 (Elsevier, 2005).

9 Piazza, G., Stephanou, P. J. & Pisano, A. P. Piezoelectric aluminum nitride vibrating contour-mode MEMS resonators. *J. Microelectromech. Syst.* **15**, 1406-1418, doi:10.1109/Jmems.2006.886012 (2006).

10 Hao, Z. & Ayazi, F. Support loss in the radial bulk-mode vibrations of center-supported micromechanical disk resonators. *Sens. Actuators, A* **134**, 582-593 (2007).

11 Kun, W., Ark-Chew, W. & Nguyen, C. T. C. VHF free-free beam high-Q micromechanical resonators. *J. Microelectromech. Syst.* **9**, 347-360, doi:10.1109/84.870061 (2000).

12 Sepúlveda, N., Lu, J., Aslam, D. M. & Sullivan, J. P. High-performance polycrystalline diamond micro-and nanoresonators. *J. Microelectromech. Syst.* **17**, 473-482 (2008).

13 Ansari, A., Gokhale, V. J., Thakar, V. A., Roberts, J. & Rais-Zadeh, M. Gallium nitride-on-silicon micromechanical overtone resonators and filters. in *Proc. IEEE IEDM*. 20.23.21 - 20.23.24 (2011).
14 Tabrizian, R., Rais-Zadeh, M. & Ayazi, F. Effect of phonon interactions on limiting the f.Q product of micromechanical resonators. in *Proc. Transducers Conf.*, 2131-2134 (2009).
15 Maines, J. D., Marshall, F. G., Paige, E. G. S. & Stuart, R. A. Gigahertz acousto-electric oscillations in zinc oxide. *Phys. Lett. A* **26**, 388-389, doi:http://dx.doi.org/10.1016/0375-9601(68)90391-5 (1968).
16 Ridley, B. K., Schaff, W. J. & Eastman, L. F. Hot-phonon-induced velocity saturation in GaN. *J. Appl. Phys.* **96**, 1499-1502, doi:10.1063/1.1762999 (2004).
17 Albrecht, J. D., Wang, R. P., Ruden, P. P., Farahmand, M. & Brennan, K. F. Electron transport characteristics of GaN for high temperature device modeling. *J. Appl. Phys.* **83**, 4777-4781, doi:http://dx.doi.org/10.1063/1.367269 (1998).
18 Look, D. C. *et al.* Electrical properties of bulk ZnO. *Solid State Commun* **105**, 399-401 (1998).
19 Look, D. C. Recent advances in ZnO materials and devices. *Mater. Sci. Eng., B* **80**, 383-387 (2001).
20 Albrecht, J. D., Ruden, P. P., Limpijumnong, S., Lambrecht, W. R. L. & Brennan, K. F. High field electron transport properties of bulk ZnO. *J. Appl. Phys.* **86**, 6864-6867, doi:http://dx.doi.org/10.1063/1.371764 (1999).
21 Hutson, A. R., White, D. L. & Mcfee, J. H. Ultrasonic Amplification in CdS. *Phys. Rev. Lett.* **7**, 237-240 (1961).
22 Karmann, S., Helbig, R. & Stein, R. A. Piezoelectric properties and elastic constants of 4H and 6H SiC at temperatures 4K-320K. *J.Appl.Phys.* **66**, 3922-3924, doi:10.1063/1.344477 (1989).
23 Powell, A. *et al. SiC Materials and Devices*. Vol. 1 1-43 (World Scientific Publishing Co., 2006).
24 Khan, I. A. & Cooper, J. A., Jr. Measurement of high-field electron transport in silicon carbide. *IEEE Trans. Electron Devices* **47**, 269-273, doi:10.1109/16.822266 (2000).
25 Adachi, S. *Physical Properties of III-V Semiconductor Compounds*. 17-44, 63-75, 223-263 (John Wiley & Sons, 1992).
26 Adachi, S. *GaAs and related materials*. 49-70,112-135,546-616 (World Scientific Publishing Co. , 1994).
27 Quay, R., Moglestue, C., Palankovski, V. & Selberherr, S. A temperature dependent model for the saturation velocity in semiconductor materials. *Mater. Sci. Semicond. Process.* **3**, 149-155, doi:http://dx.doi.org/10.1016/S1369-8001(00)00015-9 (2000).
28 Jena, D., Alpay, S. P. & Mantese, J. in *Polarization Effects in Semiconductors* (eds Colin Wood & Debdeep Jena) Ch. 7, 307-372 (Springer US, 2008).